Science Advances
AAAS

advances.sciencemag.org/cgi/content/full/6/27/eabb2958/DC1

# Supplementary Materials for

## Temperature-resilient solid-state organic artificial synapses for neuromorphic computing

A. Melianas*, T. J. Quill, G. LeCroy, Y. Tuchman, H. v. Loo, S. T. Keene, A. Giovannitti, H. R. Lee, I. P. Maria, I. McCulloch, A. Salleo*

*Corresponding author. Email: armantas.melianas@stanford.edu (A.M.); asalleo@stanford.edu (A.S.)

Published 3 July 2020, *Sci. Adv.* **6**, eabb2958 (2020)
DOI: 10.1126/sciadv.abb2958

**This PDF file includes:**

Supplementary Materials and Methods
Figs. S1 to S7
Note S1
References

## Supplementary Materials

### Materials and Methods

**Materials.** 1-Ethyl-3-methylimidazolium tetrafluoroborate (EMIM:$BF_4$) was purchased from Iolitec (>98 % grade). The EMIM:$BF_4$ PVDF-HFP ion gel was prepared in the same way as EIM:TFSI and EMIM:TFSI based ion gels described in the Materials and Methods of the main text. The block copolymers poly(styrene)-b-poly(ethyl acrylate)-b-poly(styrene) (PS-PEA-PS), poly(styrene)-b-poly(ethylene oxide)-b-poly(styrene) (PS-PEO-PS) and poly(styrene)-b-poly(methyl methacrylate)-b-poly(styrene) (PS-PMMA-PS) were purchased from Polymer Source, Inc. In the case of PS-PEA-PS, the molecular masses of PS and PEA blocks were $M_n$ = 1 kg mol$^{-1}$ and $M_n$ = 69 kg mol$^{-1}$, respectively. In the case of PS-PEO-PS, the molecular masses of PS and PEO blocks were $M_n$ = 10.5 kg mol$^{-1}$ and $M_n$ = 48 kg mol$^{-1}$, respectively. In the case of PS-PMMA-PS, the molecular masses of PS and PMMA blocks were $M_n$ = 3.5 kg mol$^{-1}$ and $M_n$ = 42 kg mol$^{-1}$, respectively. Block copolymer ion gels were prepared in ambient by dissolving the chosen polymeric insulator and the ionic liquid (1:4 w/w) in dichloromethane with the following proportions: 4.2 wt% ionic liquid 1.05 wt% polymer and 94.75 wt% solvent. The resulting ion gel solutions were stirred at 40 ºC for at least 30 min and then drop cast onto the pre-patterned organic semiconductor channel/gate. The above block copolymer ion gels are similar to those reported previously (*30*).

**XPS.** Depth profile characterization was performed using PHI VersaProbe 3 X-ray photoelectron spectrometer with a monochromatized Al source (1486 eV; 50 W; 200 μm spot size). The elemental regions collected were F1s, O1s, In3d5, N1s, C1s, S2p, and Si2p. Sputtering was performed using an $Ar_{2500}^+$ gas cluster ion gun at 10 kV, 30 nA and rastered over a 2 x 2 mm area. All samples were neutralized with an electron flood gun and low energy $Ar^+$ ions to prevent sample charging. The angle between the sample surface and the detector was 45° for all collections. Atomic concentrations were determined using the CasaXPS software according to peak areas and relative sensitivity factors of the species present. The spectra were background subtracted using a Shirley-type background and smoothed using the three-point linear Savitzky-Golay method. Gaussian-Lorentzian lineshapes were used for peak fitting. The S2p peaks attributed to thiophene were differentiated from those of PSS and TFSI on basis of their binding energies as described in ref. (*31*).

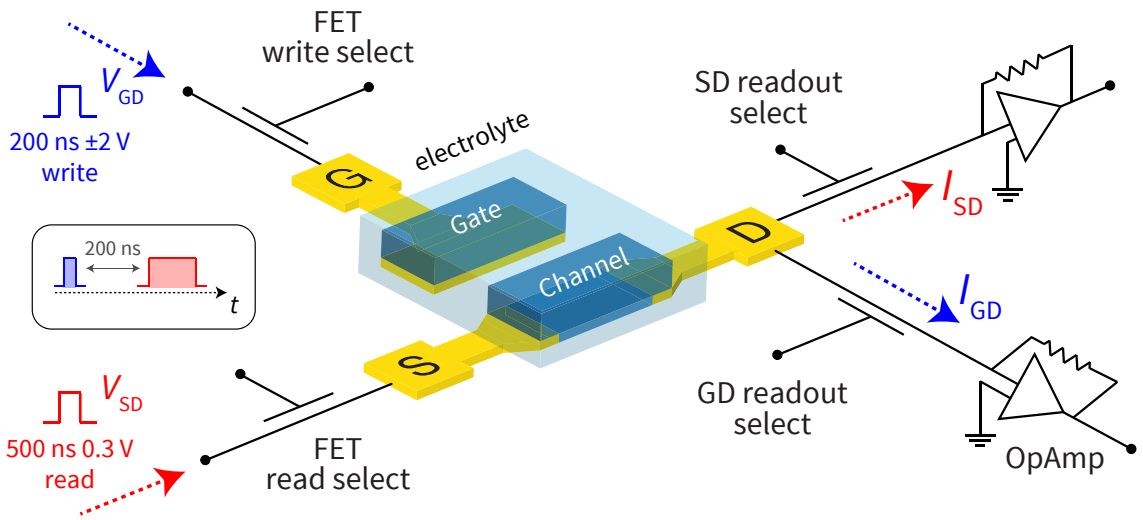


**Fig. S1. Organic ECRAM measurement schematic.** We use an access transistor at the ECRAM gate as the write select and an access transistor at the ECRAM source as the read select. The select transistors are synchronized in time with their corresponding write (blue) and read (red) pulses, and are turned ON (allowing current flow) for the duration of these pulses. The above schematic shows the pulse durations used in the <1 µs write-read cycling measurement (Fig. 3c). In the example shown above, the write select transistor is turned ON for the ~200 ns duration of the write pulse (blue) and is turned OFF (no current flow) immediately after. The read pulse is delayed by ~200 ns following a write, as schematically shown in the inset (black rectangle). Following the ~200 ns write-read delay, the read select transistor is turned ON for the ~500 ns duration of the read pulse and is turned OFF immediately after. The ECRAM gate-drain current (i.e. write current) and the source-drain conductance are measured using operational amplifiers (marked as OpAmp). To ensure accurate readout, we use two additional switches: gate-drain (GD) readout select and source-drain (SD) readout select. The GD readout select is ON (allowing current flow) for the duration of the write pulse and is turned OFF (no current flow) immediately after. The SD readout select is synced in a similar manner with the read pulse: the SD readout select is ON (allowing current flow) for the duration of the read pulse and is turned OFF (no current flow) immediately after. The measured source-drain current $I_{SD}$ (converted from the measured voltage by the OpAmp using a known gain) is then used to obtain the channel conductance $G_{SD}$, while the gate-drain current $I_{GD}$ is integrated for the duration of the write pulse to obtain the amount of injected charge $\Delta Q$ per write pulse.

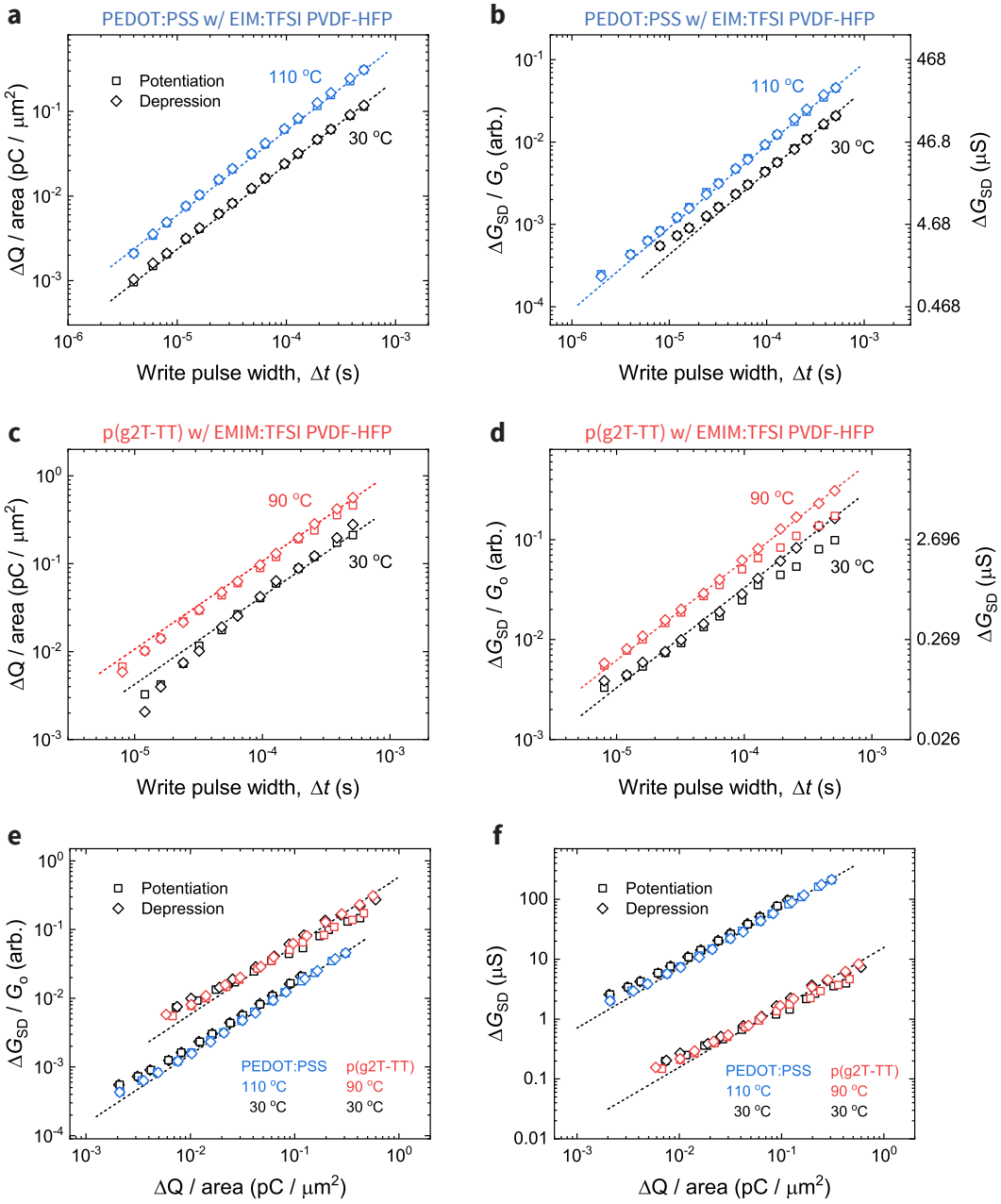


**Fig. S2. Dependence of injected charge $\Delta Q$ and conductance update $\Delta G_{SD}$ on write pulse duration as well as temperature.** To directly compare PEDOT:PSS (panels a-b) and p(g2T-TT) (panels c-d), we normalize $\Delta G_{SD}$ by the median channel conductance $G_o$ at 30 °C and normalize $\Delta Q$ by the ECRAM channel area. The increase in the amount of injected charge $\Delta Q$ / area per write pulse as well as the corresponding conductance update $\Delta G_{SD}$ / $G_o$ per write pulse are found to increase linearly with increasing write pulse duration $\Delta t$ (dashed lines are linear fits). The above panels are used to obtain the scaling of $\Delta G_{SD}$ / $G_o$ versus $\Delta Q$ / area (panel e), whereas panel f shows the same scaling in absolute conductance units, i.e. $\Delta G_{SD}$ versus $\Delta Q$ / area. We find that the scaling of $\Delta G_{SD}$ / $G_o$ versus $\Delta Q$ / area is temperature-independent, as also shown in the main text Fig. 2c. This means that the observed increase in $\Delta G_{SD}$ / $G_o$ with increasing temperature (panels b and d) originates from an increase in the amount of injected charge $\Delta Q$ / area (panels a and c). This is confirmed by time-resolved measurements of the write current transient in the main text Fig. 2d.

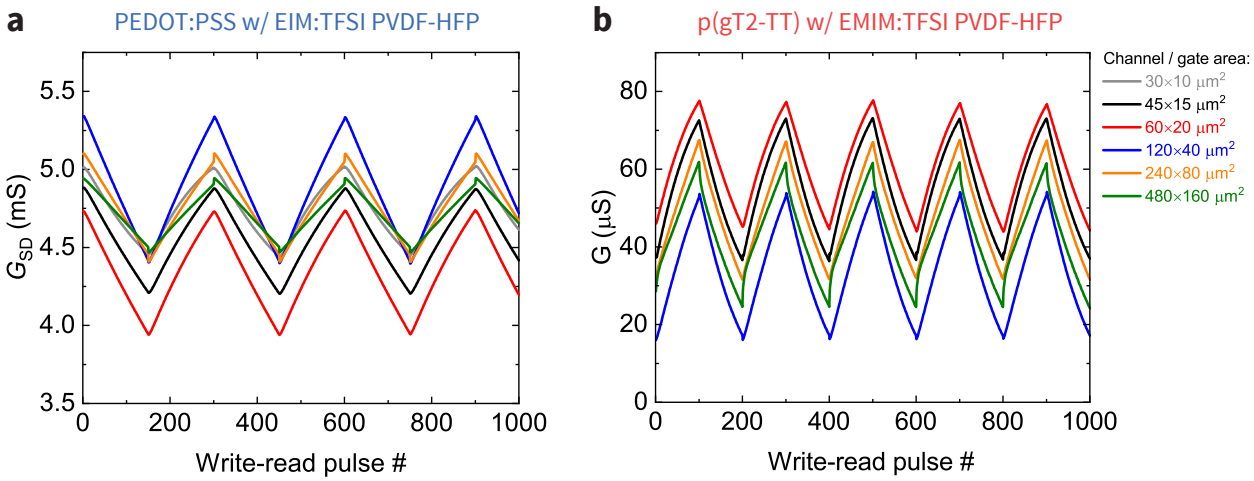


**Fig. S3. Device-to-device variability.** Switching characteristics of various sized (**a**) PEDOT:PSS EIM:TFSI PVDF-HFP and (**b**) p(g2T-TT) EMIM:TFSI PVDF-HFP devices operated using scaled write duration, shown in the switching speed scaling plots (Figs. 3a-b). ECRAM channel/gate have the same area and are separated by the indicated second dimension, resulting in a square cell (e.g. 45x15 μm$^2$ channel/gate are separated by 15 μm, resulting in a 45x45 μm$^2$ cell). The write pulse duration was adjusted according to channel area such that all devices would span the same dynamic range. For example, whereas a 2x conductance modulation can be obtained in a 240x80 μm$^2$ p(g2T-TT) channel (orange) when using 100x ±1 V 600 ns programming pulses, a similar 2x modulation can be attained in a 45x15 μm$^2$ channel (black) using 100x ±1 V 20 ns programming pulses, i.e. using 30x shorter write pulses, matching the 30x decrease in channel area. The observed device-to-device variability is not a materials property, as the ECRAMs in this work were fabricated in a relatively uncontrolled multi-purpose university cleanroom environment. We anticipate that device-to-device variability can be substantially reduced using better suited/equipped fabrication facilities as well as using new and/or optimized ECRAM fabrication methods.

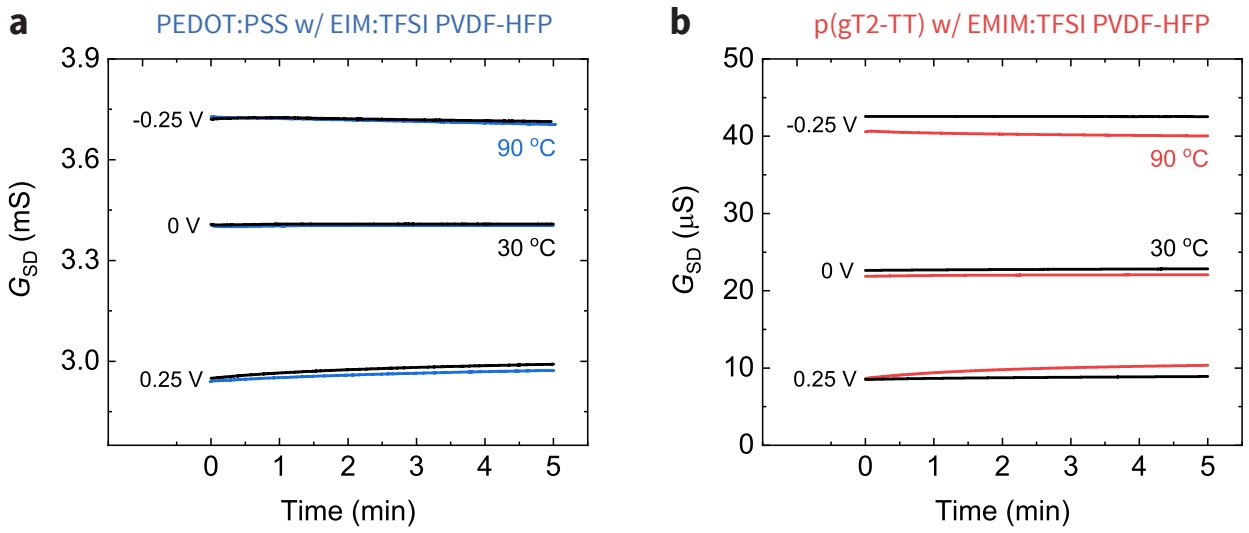


**Fig. S4. State retention.** State retention of (**a**) PEDOT:PSS EIM:TFSI PVDF-HFP and (**b**) p(g2T-TT) EMIM:TFSI PVDF-HFP devices at the indicated temperature under $2x10^{-4}$ mbar vacuum. To estimate state retention, the devices were first programmed to a desired source-gate voltage $V_{SG}$, for example $V_{SG}$ = -0.25 V, followed by leaving the gate floating, and continuously measuring the source-drain conductance $G_{SD}$. For 50x states, the estimated state retention for PEDOT:PSS EIM:TFSI PVDF-HFP is ~1 min both at 30 °C and at 90 °C, while for p(g2T-TT) EMIM:TFSI PVDF-HFP the state retention is >5 min at 30 °C and ~1 min at 90 °C. In both materials systems the state retention is mostly limited by the faster discharge at 0.25 V.

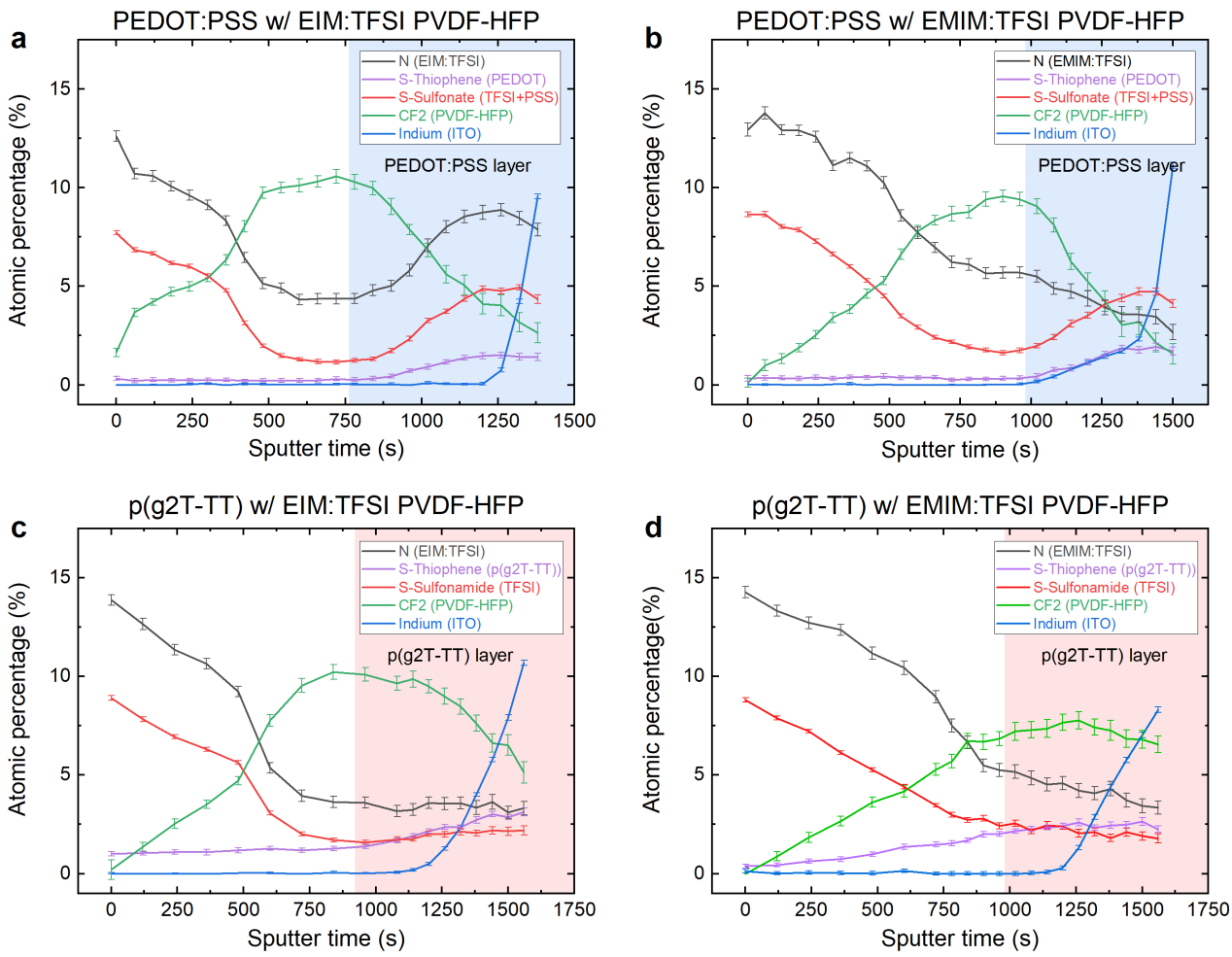


**Fig. S5. XPS reveals ionic liquid uptake by the organic semiconductor channel prior to electrochemical gating.** XPS depth profiles of PEDOT:PSS films with (**a**) EIM:TFSI PVDF-HFP and (**b**) EMIM:TFSI PVDF-HFP ion gels on top, and p(g2T-TT) films with (**c**) EIM:TFSI PVDF-HFP and (**d**) EMIM:TFSI PVDF-HFP ion gels on top. The N1s signal from both the imidazolium cation and the TFSI anion serves as a unique ionic liquid marker. In all cases, the increase in S-thiophene concentration (purple), originating from the organic semiconductor, and the coexistence of N1s peaks (black) confirm the presence of ionic liquid throughout the bulk of the channel material. In the case of PEDOT:PSS (top panels a-b), the rise in S-sulfonate concentration is due to the high concentration of PSS. In the case of p(g2T-TT) (bottom panels c-d), the S2p peak, attributed to the sulfonamide group of TFSI, serves as a secondary ionic liquid marker. The error bars represent one standard deviation of the atomic concentration based on Monte Carlo analysis performed using CasaXPS software, see Materials and Methods in Supplementary Materials for details. The shaded regions are a guide to the eye, indicating the estimated position of the PEDOT:PSS (blue) or p(g2T-TT) (red) layers, whereas the non-shaded regions correspond to the ion gel electrolyte.

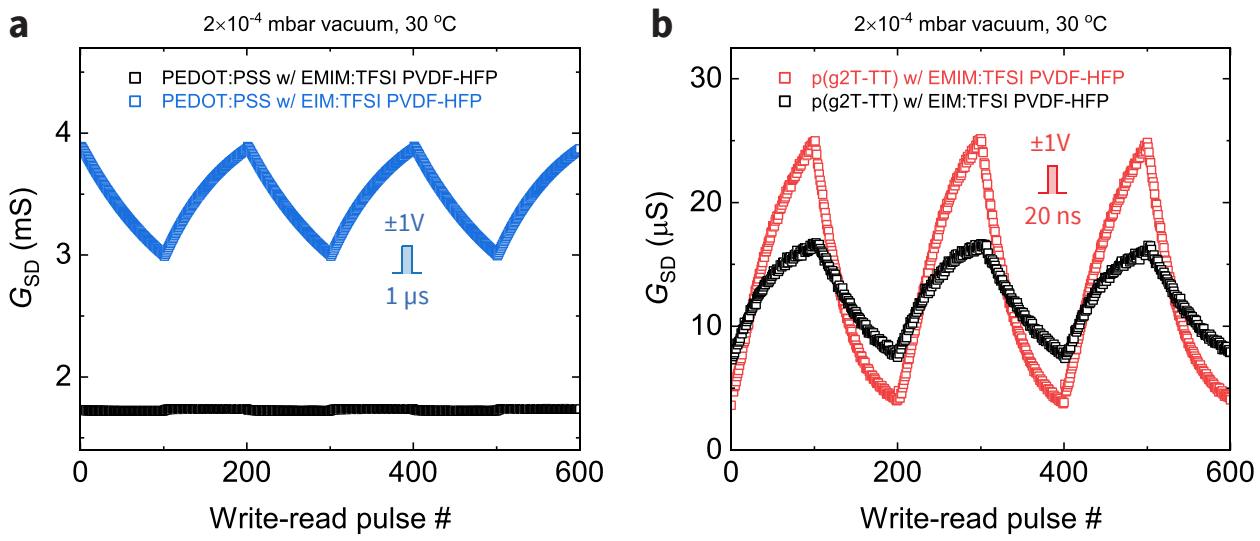


**Fig. S6. Comparison of ECRAMs using EMIM:TFSI versus EIM:TFSI based ion gels.** Cycling characteristics of ECRAMs with (**a**) PEDOT:PSS and (**b**) p(g2T-TT) as the channel/gate material, and EMIM:TFSI PVDF-HFP or EIM:TFSI PVDF-HFP as the ion gel electrolyte. PEDOT:PSS devices were cycled using ±1 V 1 µs write pulses, whereas ±1 V 20 ns write pulses were used in the case of p(g2T-TT) devices due to their higher switching speed. PEDOT:PSS devices using the aprotic ionic liquid EMIM:TFSI are barely operational (Fig. S6a, black trace) while those made with the protic (*26*, *27*) EIM:TFSI exhibit excellent performance (Figs. S6a, blue trace). The higher dynamic range in PEDOT:PSS devices based on the protic ion gel EIM:TFSI PVDF-HFP suggests that protons play an important role in the resistive switching of our ECRAMs. p(g2T-TT) devices on the other hand show excellent performance with both ion gels (Fig. S6b), suggesting the need for a more detailed understanding of the switching mechanisms and their relationship to proton transport that are beyond the scope of this work. The measurements were performed at 30 °C under 2x10$^{-4}$ mbar vacuum.

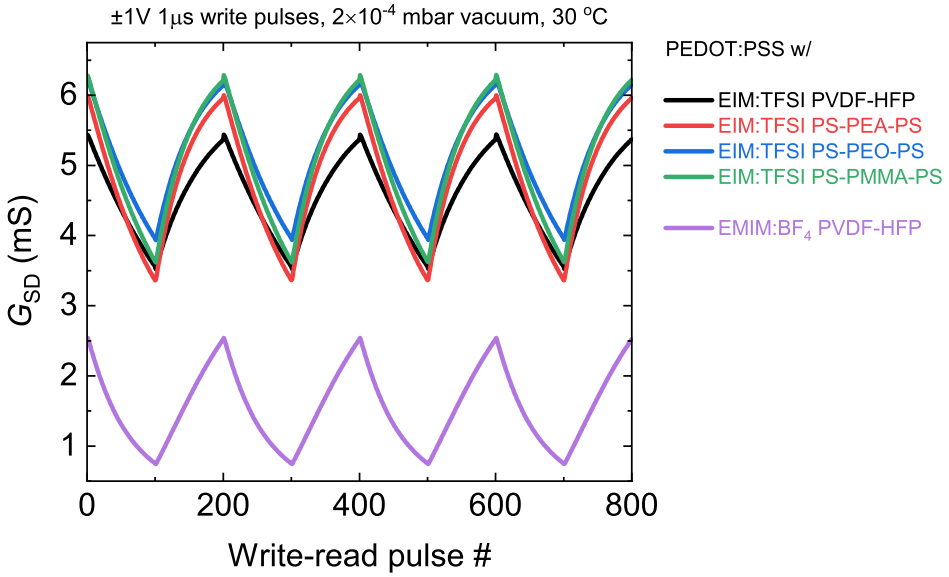


**Fig. S7. Organic ECRAMs can also be made using various block copolymers as well as other ionic liquids.** Cycling characteristics of ECRAMs with PEDOT:PSS as the channel/gate material and the indicated ion gel as electrolyte: 1-Ethyl-3-methylimidazolium tetrafluoroborate (EMIM:$BF_4$) gelated with PVDF-HFP or EIM:TFSI gelated with block copolymers such as poly(styrene)-b-poly(ethyl acrylate)-b-poly(styrene) (PS-PEA-PS), poly(styrene)-b-poly(ethylene oxide)-b-poly(styrene) (PS-PEO-PS) or poly(styrene)-b-poly(methyl methacrylate)-b-poly(styrene) (PS-PMMA-PS), see Materials and Methods in Supplementary Materials for details. The devices were cycled using ±1 V 1 μs write pulses at 30 °C under $2x10^{-4}$ mbar vacuum.

**Note S1. ECRAM channel carrier mobility is temperature-independent in the temperature range studied in this work.** The increase in the amount of injected charge per write pulse $\Delta Q$ at elevated temperature leads to a corresponding increase in the conductance change per write pulse $\Delta G_{SD}$ (Supplementary Fig. S2). However, we find that the scaling of $\Delta G_{SD}$ versus $\Delta Q$ is close to temperature-independent (Supplementary Fig. S2). This means that the increase in $\Delta G_{SD}$ at elevated temperature is solely due an increase in $\Delta Q$, as confirmed by time-resolved measurements of charging during the write pulse (Fig. 2d). As a result, we conclude that carrier mobility is nearly temperature-independent in the temperature range studied here.

If the carrier mobility was decreasing with temperature, $\Delta G_{SD}$ versus $\Delta Q$ would be decreasing with temperature, which is not the case. Instead, in view of the faster charging at elevated temperature (Fig. 2d), it appears that ion mobility increases with increasing temperature, leading to a larger $\Delta Q$ for identical pulse length when the temperature is increased (Supplementary Fig. S2).

In addition, organic (semi)conductors are typically cooled below 300K when measuring the charge carrier mobility dependence vs temperature. Due to the thermally activated nature of hopping transport in disordered organic solids, carrier mobility is strongly temperature-dependent and increasing with temperature in this regime. In contrast, here the samples are heated above 300K. In this regime, the carrier mobility is significantly less temperature dependent and may even plateau, see ref. (*32*) for an example where thermally stable organic semiconductors were investigated and show this behavior. At very high temperatures (>100 ºC) the carrier mobility may appear to decrease, but this may be due to sample degradation or morphological changes past glass transition rather than charge transport physics. In view of Fig. 2c results, carrier mobility is nearly temperature-independent in the regime studied in this work, similar to ref. (*32*).

**REFERENCES AND NOTES**


1. X. Xu, Y. Ding, S. X. Hu, M. Niemier, J. Cong, Y. Hu, Y. Shi, Scaling for edge inference of deep neural networks. *Nat. Electron.* **1**, 216–222 (2018).
2. G. W. Burr, R. M. Shelby, C. di Nolfo, J. W. Jang, R. S. Shenoy, P. Narayanan, K. Virwani, E. U. Giacometti, B. Kurdi, H. Hwang, in *2014 IEEE International Electron Devices Meeting* (IEEE, 2014), pp. 29.5.1-29.5.4.
3. M. Hu, C. E. Graves, C. Li, Y. Li, N. Ge, E. Montgomery, N. Davila, H. Jiang, R. S. Williams, J. J. Yang, Q. Xia, J. P. Strachan, Memristor-based analog computation and neural network classification with a dot product engine. *Adv. Mater.* **30**, 1705914 (2018).
4. S. Agarwal, S. J. Plimpton, D. R. Hughart, A. H. Hsia, I. Richter, J. A. Cox, C. D. James, M. J. Marinella, in *Proceedings of the International Joint Conference on Neural Networks* (IEEE, 2016), pp. 929–938.
5. H. Tsai, S. Ambrogio, P. Narayanan, R. M. Shelby, G. W. Burr, Recent progress in analog memory-based accelerators for deep learning. *J. Phys. D Appl. Phys.* **51**, 283001 (2018).
6. Y. van de Burgt, E. Lubberman, E. J. Fuller, S. T. Keene, G. C. Faria, S. Agarwal, M. J. Marinella, A. Alec Talin, A. Salleo, A non-volatile organic electrochemical device as a low-voltage artificial synapse for neuromorphic computing. *Nat. Mater.* **16**, 414–418 (2017).
7. E. J. Fuller, F. El Gabaly, F. Léonard, S. Agarwal, S. J. Plimpton, R. B. Jacobs-Gedrim, C. D. James, M. J. Marinella, A. A. Talin, Li-ion synaptic transistor for low power analog computing. *Adv. Mater.* **29**, 1604310 (2017).
8. J. Tang, D. Bishop, S. Kim, M. Copel, T. Gokmen, T. Todorov, S. Shin, K. T. Lee, P. Solomon, K. Chan, W. Haensch, J. Rozen, in *International Electron Devices Meeting, IEDM* (IEEE, 2019), pp. 13.1.1–13.1.4.
9. E. J. Fuller, S. T. Keene, A. Melianas, Z. Wang, S. Agarwal, Y. Li, Y. Tuchman, C. D. James, M. J. Marinella, J. J. Yang, A. Salleo, A. A. Talin, Parallel programming of an ionic floating-gate memory array for scalable neuromorphic computing. *Science* **364**, 570–574 (2019).
10. M. T. Sharbati, Y. Du, J. Torres, N. D. Ardolino, M. Yun, F. Xiong, Low-power, electrochemically tunable graphene synapses for neuromorphic computing. *Adv. Mater.* **30**, 1802353 (2018).
11. C. Sen Yang, D. S. Shang, N. Liu, E. J. Fuller, S. Agrawal, A. A. Talin, Y. Q. Li, B. G. Shen, Y. Sun, All-solid-state synaptic transistor with ultralow conductance for neuromorphic computing. *Adv. Funct. Mater.* **28**, 1804170 (2018).

12. Y. Li, E. J. Fuller, S. Asapu, S. Agarwal, T. Kurita, J. J. Yang, A. A. Talin, Low-voltage, CMOS-free synaptic memory based on $Li_XTiO_2$ redox transistors. *ACS Appl. Mater. Interfaces* **11**, 38982–38992 (2019).
13. K. A. Mauritz, R. B. Moore, State of understanding of Nafion. *Chem. Rev.* **104**, 4535–4585 (2004).
14. K. D. Kreuer, S. J. Paddison, E. Spohr, M. Schuster, Transport in proton conductors for fuel-cell applications: Simulations, elementary reactions, and phenomenology. *Chem. Rev.* **104**, 4637–4678 (2004).
15. K. H. Lee, M. S. Kang, S. Zhang, Y. Gu, T. P. Lodge, C. D. Frisbie, "Cut and stick" rubbery ion gels as high capacitance gate dielectrics. *Adv. Mater.* **24**, 4457–4462 (2012).
16. A. Giovannitti, D.-T. Sbircea, S. Inal, C. B. Nielsen, E. Bandiello, D. A. Hanifi, M. Sessolo, G. G. Malliaras, I. McCulloch, J. Rivnay, Controlling the mode of operation of organic transistors through side-chain engineering. *Proc. Natl. Acad. Sci. U.S.A.* **113**, 12017–12022 (2016).
17. Y. Van De Burgt, A. Melianas, S. T. Keene, G. Malliaras, A. Salleo, Organic electronics for neuromorphic computing. *Nat. Electron.* **1**, 386–397 (2018).
18. M. Lanza, H.-S. S. P. Wong, E. Pop, D. Ielmini, D. Strukov, B. C. Regan, L. Larcher, M. A. Villena, J. J. Yang, L. Goux, A. Belmonte, Y. Yang, F. M. Puglisi, J. Kang, B. Magyari-Köpe, E. Yalon, A. Kenyon, M. Buckwell, A. Mehonic, A. Shluger, H. Li, T. H. Hou, B. Hudec, D. Akinwande, R. Ge, S. Ambrogio, J. B. Roldan, E. Miranda, J. Suñe, K. L. Pey, X. Wu, N. Raghavan, E. Wu, W. D. Lu, G. Navarro, W. Zhang, H. Wu, R. Li, A. Holleitner, U. Wurstbauer, M. C. Lemme, M. Liu, S. Long, Q. Liu, H. Lv, A. Padovani, P. Pavan, I. Valov, X. Jing, T. Han, K. Zhu, S. Chen, F. Hui, Y. Shi, Recommended methods to study resistive switching devices. *Adv. Electron. Mater.* **5**, 1800143 (2019).
19. C. Zhao, C. Z. Zhao, S. Taylor, P. R. Chalker, Review on non-volatile memory with high-*k* dielectrics: Flash for generation beyond 32 nm. *Materials (Basel).* **7**, 5117–5145 (2014).
20. H. Tokuda, K. Hayamizu, K. Ishii, M. A. B. H. Susan, M. Watanabe, Physicochemical properties and structures of room temperature ionic liquids. 2. variation of alkyl chain length in imidazolium cation. *J. Phys. Chem. B* **109**, 6103–6110 (2005).
21. S. Zhang, K. H. Lee, C. D. Frisbie, T. P. Lodge, Ionic conductivity, capacitance, and viscoelastic properties of block copolymer-based ion gels. *Macromolecules* **44**, 940–949 (2011).
22. S. T. Keene, A. Melianas, Y. van de Burgt, A. Salleo, Mechanisms for enhanced state retention and stability in redox-gated organic neuromorphic devices. *Adv. Electron. Mater.* **5**, 1800686 (2019).

23. S. Ambrogio, P. Narayanan, H. Tsai, R. M. Shelby, I. Boybat, C. Di Nolfo, S. Sidler, M. Giordano, M. Bodini, N. C. P. Farinha, B. Killeen, C. Cheng, Y. Jaoudi, G. W. Burr, Equivalent-accuracy accelerated neural-network training using analogue memory. *Nature* **558**, 60–67 (2018).
24. S. T. Keene, A. Melianas, E. J. Fuller, Y. van de Burgt, A. A. Talin, A. Salleo, Optimized pulsed write schemes improve linearity and write speed for low-power organic neuromorphic devices. *J. Phys. D Appl. Phys.* **51**, 224002 (2018).
25. G. D. Spyropoulos, J. N. Gelinas, D. Khodagholy, Internal ion-gated organic electrochemical transistor: A building block for integrated bioelectronics. *Sci. Adv.* **5**, eaau7378 (2019).
26. N. Yaghini, L. Nordstierna, A. Martinelli, Effect of water on the transport properties of protic and aprotic imidazolium ionic liquids-an analysis of self-diffusivity, conductivity, and proton exchange mechanism. *Phys. Chem. Chem. Phys.* **16**, 9266–9275 (2014).
27. T. L. Greaves, C. J. Drummond, Protic ionic liquids: Properties and applications. *Chem. Rev.* **108**, 206–237 (2008).
28. X. Wu, J. J. Hong, W. Shin, L. Ma, T. Liu, X. Bi, Y. Yuan, Y. Qi, T. W. Surta, W. Huang, J. Neuefeind, T. Wu, P. A. Greaney, J. Lu, X. Ji, Diffusion-free Grotthuss topochemistry for high-rate and long-life proton batteries. *Nat. Energy* **4**, 123–130 (2019).
29. M. M. S. Aly, M. Gao, G. Hills, C. S. Lee, G. Pitner, M. M. Shulaker, T. F. Wu, M. Asheghi, J. Bokor, F. Franchetti, K. E. Goodson, C. Kozyrakis, I. Markov, K. Olukotun, L. Pileggi, E. Pop, J. Rabaey, C. Ré, H. S. P. Wong, S. Mitra, Energy-efficient abundant-data computing: The N3XT 1,000. *Computer* **48**, 24–33 (2015).
30. B. Tang, S. P. White, C. D. Frisbie, T. P. Lodge, Synergistic increase in ionic conductivity and modulus of triblock copolymer ion gels. *Macromolecules* **48**, 4942–4950 (2015).
31. G. Greczynski, T. Kugler, M. Keil, W. Osikowicz, M. Fahlman, W. R. Salaneck, Photoelectron spectroscopy of thin films of PEDOT-PSS conjugated polymer blend: A mini-review and some new results. *J. Electron Spectros. Relat. Phenomena* **121**, 1–17 (2001).
32. A. Gumyusenge, D. T. Tran, X. Luo, G. M. Pitch, Y. Zhao, K. A. Jenkins, T. J. Dunn, A. L. Ayzner, B. M. Savoie, J. Mei, Semiconducting polymer blends that exhibit stable charge transport at high temperatures. *Science* **362**, 1131–1134 (2018).